



Synthesis of $\text{LiTi}_2(\text{PO}_4)_3$ -acetylene black nanocomposites for lithium ion batteries by the polyvinyl alcohol assisted sol–gel method and ball-milling

Meng Zhou, Li Liu*, Lanhua Yi, Zhenhua Yang, Sha Mao, Yunan Zhou, Tingting Hu, Yang Yang, Bowen Shen, Xianyou Wang**

School of Chemistry, Key Laboratory of Environmentally Friendly Chemistry and Applications of Ministry of Education, Xiangtan University, Xiangtan 411105, China

HIGHLIGHTS

- ▶ $\text{LiTi}_2(\text{PO}_4)_3$ can be synthesized by PVA sol–gel method at a low temperature successfully.
- ▶ $\text{LiTi}_2(\text{PO}_4)_3$ -acetylene black nanocomposites was synthesized by a simple ball-milling.
- ▶ $\text{LiTi}_2(\text{PO}_4)_3$ -acetylene black nanocomposite with 15 wt.% acetylene black shows excellent electrochemical properties.

ARTICLE INFO

Article history:

Received 28 July 2012

Received in revised form

16 November 2012

Accepted 16 January 2013

Available online 6 February 2013

Keywords:

Lithium titanium phosphate

Lithium ion batteries

Ball-milling

Sol–gel method

ABSTRACT

Lithium titanium phosphate ($\text{LiTi}_2(\text{PO}_4)_3$) has been successfully synthesized by a polyvinyl alcohol (PVA) assisted sol–gel method. To further improve its electrochemical properties, a ball-milling process with various amount of acetylene black (AB) has been used to form $\text{LiTi}_2(\text{PO}_4)_3$ -AB nanocomposites (the weight ratio of acetylene black is 5 wt.%, 10 wt.%, 15 wt.% and 20 wt.%). The samples are characterized by X-ray diffraction (XRD), scanning electron microscopy (SEM), and transmission electron microscopy (TEM). Electrochemical performance of the samples is characterized by the charge–discharge test, cyclic voltammetry (CV), electrochemical impedance spectroscopic studies (EIS), and galvanostatic intermittent titration technique (GITT). The results show that the ball-milling process enables $\text{LiTi}_2(\text{PO}_4)_3$ nanoparticles to network with conductive acetylene black, which offers better electrochemical performance. Especially, $\text{LiTi}_2(\text{PO}_4)_3$ -AB nanocomposite with 15 wt.% acetylene black shows the best electrochemical properties, which delivers the highest specific capacity and the best cycle performance. Besides, the thermodynamics properties of as-prepared samples are also been studied.

© 2013 Elsevier B.V. All rights reserved.

1. Introduction

The Na^+ superionic conductor (NASICON) materials are good ionic conductors when serving as solid-state electrolytes. The Nasicon-type lithium titanium phosphate ($\text{LiTi}_2(\text{PO}_4)_3$) has attracted a significant interest for applications in all-solid-state rechargeable lithium ion batteries as solid lithium ion electrolytes [1,2]. Meantime, $\text{LiTi}_2(\text{PO}_4)_3$ can also be used as lithium-storage materials in rechargeable lithium batteries, based on their structural characteristics. $\text{LiTi}_2(\text{PO}_4)_3$ has a rhombohedral (space group: $R\bar{3}c$) structure with an open three-dimensional framework of TiO_6 octahedra sharing all corners with PO_4 tetrahedra and vice versa. The interstitials and conduction channels are generated along the c -axis direction, in

which Li^+ ions occupy the interstitial sites. Consequently, the Li^+ ions can move easily along the conduction channels.

In the late 1980s, Delmas was the first to show the possibility of lithium insertion into $\text{LiTi}_2(\text{PO}_4)_3$ [3–7]. $\text{LiTi}_2(\text{PO}_4)_3$ may reversibly insert two lithium ions, operating on the $\text{Ti}^{4+}/\text{Ti}^{3+}$ at 2.48 V vs Li^+/Li , according to a two-phase mechanism between $\text{LiTi}_2(\text{PO}_4)_3$ and $\text{Li}_3\text{Ti}_2(\text{PO}_4)_3$ [3,8,9]. $\text{LiTi}_2(\text{PO}_4)_3$ is an interesting cathode electrode material for 2.5–2.6 V polymer lithium batteries containing Li at the negative electrode [3], and it is also a promising anode electrode material in aqueous rechargeable lithium batteries [8–10]. However, the disadvantages, including the low intrinsic electronic conductivity of these 3-D phosphates [11–13], prevent $\text{LiTi}_2(\text{PO}_4)_3$ from being widely used in large-scale applications. In addition, the most common and traditional method to prepare $\text{LiTi}_2(\text{PO}_4)_3$ is the solid-state reaction synthesis. This approach, nevertheless, suffers from the problems of complicated producing processes including grinding, ball-milling, and subsequent heat treatment generally at 1000 °C until the crystalline $\text{LiTi}_2(\text{PO}_4)_3$ formed [9,10,14], which

* Corresponding author. Tel.: +86 731 58292206; fax: +86 731 58292477.

** Corresponding author.

E-mail addresses: liulili1203@yahoo.com.cn (L. Liu), wxianyou@yahoo.com (X. Wang).

inevitably induces high energy consumption and large particle sizes of the product.

It has been demonstrated by many researchers that nano-structuring the active material and the conductive agent is a promising strategy for fabricating high-performance electrode materials [15–17]. Hybrid electrodes composed of LiFePO_4 and nano-graphite platelet (NGP) exhibited excellent electrochemical properties, which was due to NGP framework afforded easy electron transport and a high degree of stability [15]. It was also found by Badway et al. that the practical electroactivity of electrically insulating iron fluoride was enhanced through forming carbon-metal fluoride nanocomposites (CMFNCs) by high energy mechanical ball-milling with carbon [16]. The improved electrochemical properties are attributed to reducing the solid phase diffusion thickness for lithium ions and increasing the overall electronic conductivity for electron transport. For $\text{LiTi}_2(\text{PO}_4)_3$, Patoux and Masquelier [3] prepared $\text{LiTi}_2(\text{PO}_4)_3/\text{C}$ by solid-state method and subsequent ball-milling with 16.67 wt. % of Super P. The cell delivered discharge capacities of ~ 120 and $\sim 95 \text{ mAh g}^{-1}$ at a current density of 15 mA g^{-1} in the voltage of 2 and 3.4 V at the first cycle and after 40 cycles, respectively. Wessells et al. [18] synthesized $\text{LiTi}_2(\text{PO}_4)_3/\text{C}$ by Pechini's method followed by 4 wt.% carbon coating and observed an initial discharge capacity of 115 mAh g^{-1} with 84% capacity retention after 100 cycles at 1C rate between 2 and 3 V. Recently, carbon coated nano- $\text{LiTi}_2(\text{PO}_4)_3$ ($\text{LiTi}_2(\text{PO}_4)_3/\text{C}$) electrode was fabricated by a Pechini type polymerizable complex decomposition method at 1000°C in air, high energy ball-milling was followed, then it was dispersed in glucose and heated at 800°C in Ar atmosphere [19]. The as-prepared $\text{LiTi}_2(\text{PO}_4)_3$ by 2.3 wt.% carbon coating delivered an initial discharge capacity of 117 mAh g^{-1} at 15 mA g^{-1} between 2 and 3.4 V with 83% capacity retention after 70 cycles. As mentioned above, improvement in electron transport is achieved by carbon coating. However, the producing process of $\text{LiTi}_2(\text{PO}_4)_3/\text{C}$ composites previously reported is complicated. Besides, the electronic conductivity cannot be ameliorated effectively with a small amount of carbon, and thicker carbon coating leads to lower reversible capacity is due to hindered lithium penetration also the bulk density, which is essential for volumetric energy density, decreases with a higher amount of carbon [20].

Though the electrochemical performance of previous $\text{LiTi}_2(\text{PO}_4)_3/\text{C}$ was superior, the effect of carbon amount on cycle stability was not studied and compared in detail. In addition, further improvement in initial discharge capacity and cycle stability of $\text{LiTi}_2(\text{PO}_4)_3$, including preparation method and other modified materials, are still much in demand. In this work, we are aiming to seek the effect of carbon coating amount on discharge/charge capacity and cycle stability via an easy way. $\text{LiTi}_2(\text{PO}_4)_3$ was synthesized by a PVA assisted sol–gel method, then it was ball-milled with various amount of acetylene black to form $\text{LiTi}_2(\text{PO}_4)_3\text{-AB}$ nanocomposites. The amount of acetylene black was optimized and the crystal structure, morphology, electrochemical performance, kinetic and thermodynamic properties of synthesized nanocomposites were investigated systematically. Especially, their electrochemical performance as cathode materials with our focus on the high rate utilization and cyclic performance at room temperature in the range from 1.5 to 3.5 V were compared in detail.

2. Experimental

2.1. Sample synthesis

Certain amount of PVA was dissolved in distilled water at 90°C to form 2 wt. % PVA solutions. Then stoichiometric amount of Li_2CO_3 , TiO_2 , and $\text{NH}_4\text{H}_2\text{PO}_4$ were dispersed in the PVA solution

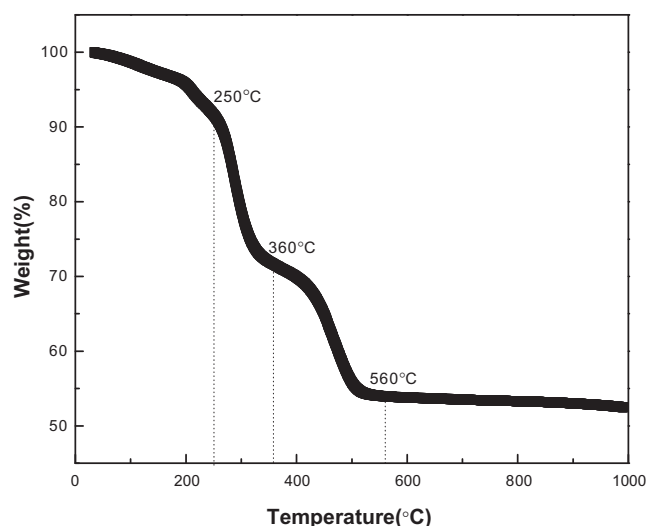


Fig. 1. TG curve of the precursor recorded from 30 to 1000°C at the heating rate of 5°C min^{-1} in N_2 atmosphere.

under constant stirring at 80°C to form an emulsion, and then the emulsion product was dried at 80°C to form the precursor. The precursor was sintered at 800°C for 12 h under an argon atmosphere to form $\text{LiTi}_2(\text{PO}_4)_3$ (named as LTP). The as-prepared $\text{LiTi}_2(\text{PO}_4)_3$ and acetylene black (the weight ratio is 95:5, 90:10, 85:15 or 80:20) were ball-milled in a planetary ball mill (PM 200) at 300 rpm for 3 h to yield $\text{LiTi}_2(\text{PO}_4)_3\text{-AB}$ nanocomposites. $\text{LiTi}_2(\text{PO}_4)_3\text{-AB}$ nanocomposites with acetylene black 5 wt.%, 10 wt.%, 15 wt.%, and 20 wt.% were named as LTP/C-1, LTP/C-2, LTP/C-3 and LTP/C-4, respectively.

2.2. Structure characterization and electrochemical measurements

The precursor was analyzed by thermogravimetry (TG) using a Thermogravimetric–differential Thermal analyzer (Standard Type High temp. Type, Rigaku). The tests were conducted in N_2 atmosphere.

The structures of synthesized samples were characterized by X-ray diffraction spectroscopy (XRD). X-ray powder diffraction data

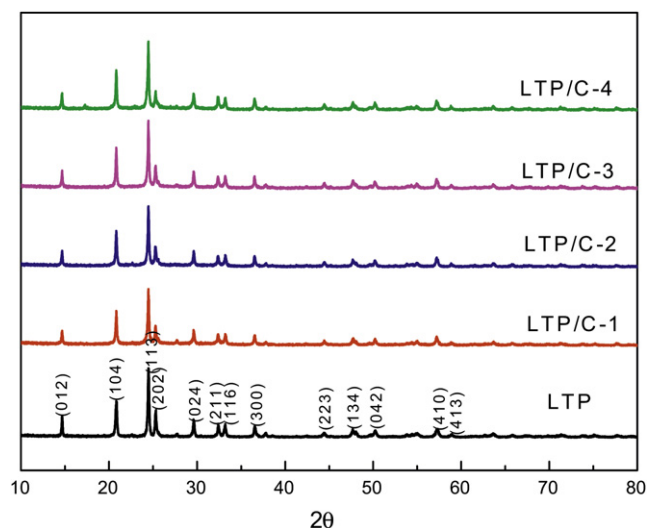


Fig. 2. XRD patterns of LTP, LTP/C-1, LTP/C-2, LTP/C-3, and LTP/C-4.

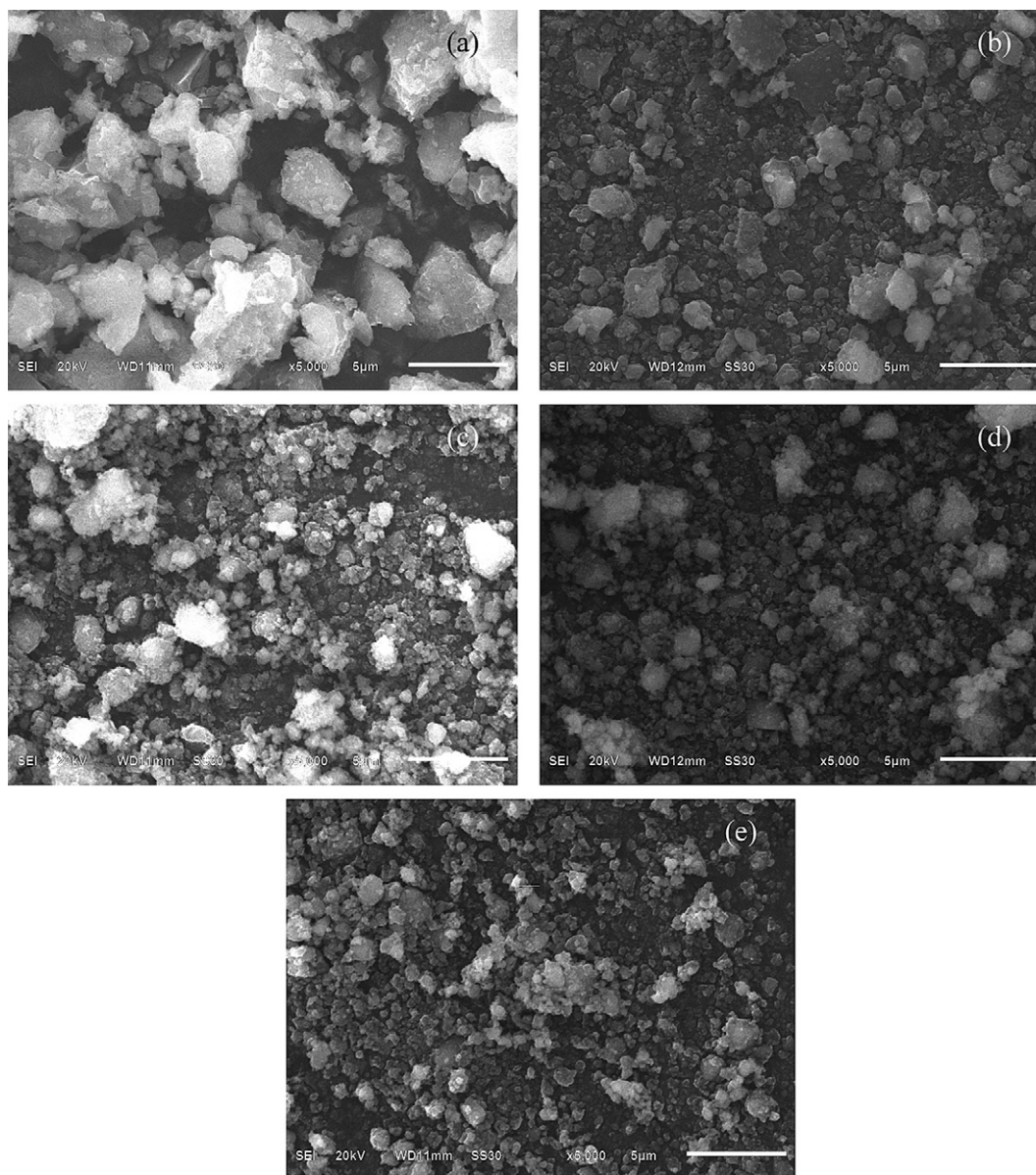


Fig. 3. SEM images of (a) LTP, (b) LTP/C-1, (c) LTP/C-2, (d) LTP/C-3, and (e) LTP/C-4.

were obtained using a Rigaku D/MAX-2500 powder diffractometer with a graphite monochromatic and Cu K α radiation ($\lambda = 0.15418$ nm) in the 2θ range of 10° – 80° .

Scanning electron microscope (SEM) images of the samples were collected on the FEG SEM Sirion scanning electron microscope, which was used to observe the particle morphology, particle size and particle size distribution. The transmission electron microscopy (TEM) images were collected using FEI Tecnai G20 transmission electron microscope at an acceleration voltage of 200 kV.

The cathodes for lithium cells were fabricated by mixing the cathode material, carbon black, and polyvinylidene fluoride (PVDF) binder in a weight ratio of 85:10:5. The testing cells were assembled with the cathodes thus fabricated, metallic lithium anode, celgard 2300 film separator and 1 M LiPF $_6$ in 1:1 ethylene carbonate (EC)/dimethyl carbonate (DMC) electrolyte. The assembly of the testing cells was carried out in an argon-filled glove box, where water and oxygen concentrations were kept less than 5 ppm. The discharge–charge cycle tests were run at different current of 0.1C,

0.5C, 1C, 2C, and 5C (140 mA g $^{-1}$ was assumed to be 1C rate) densities between 3.5 and 1.5 V. All the tests were performed at room temperature.

Cyclic voltammetry (CV) tests and EIS experiments were performed on a Zahner Zennium electrochemical workstation. CV tests were carried out at a scan rate of 1 mV s $^{-1}$ on the potential interval 1.5–3.5 V (vs. Li $^{+}$ /Li). The ac perturbation signal was ± 5 mV, and the frequency range was from 100 mHz to 10^5 Hz.

3. Results and discussion

Fig. 1 shows the thermogravimetric (TG) curve of the precursor obtained over the temperature range from room temperature (30°C) to 1000°C . Three distinct regions of weight loss are found in the regions of 30 – 250 , 250 – 360 and 360 – 560°C . The first weight loss region, i.e. before 250°C is mainly attributed to the release of little physical adsorbed water and the decomposition of NH $_4$ H $_2$ PO $_4$ (ca. 8.5 wt.%). The steep weight loss (around 19.5%), which occurs between 250 and 360°C , arises from the decomposition of PVA and

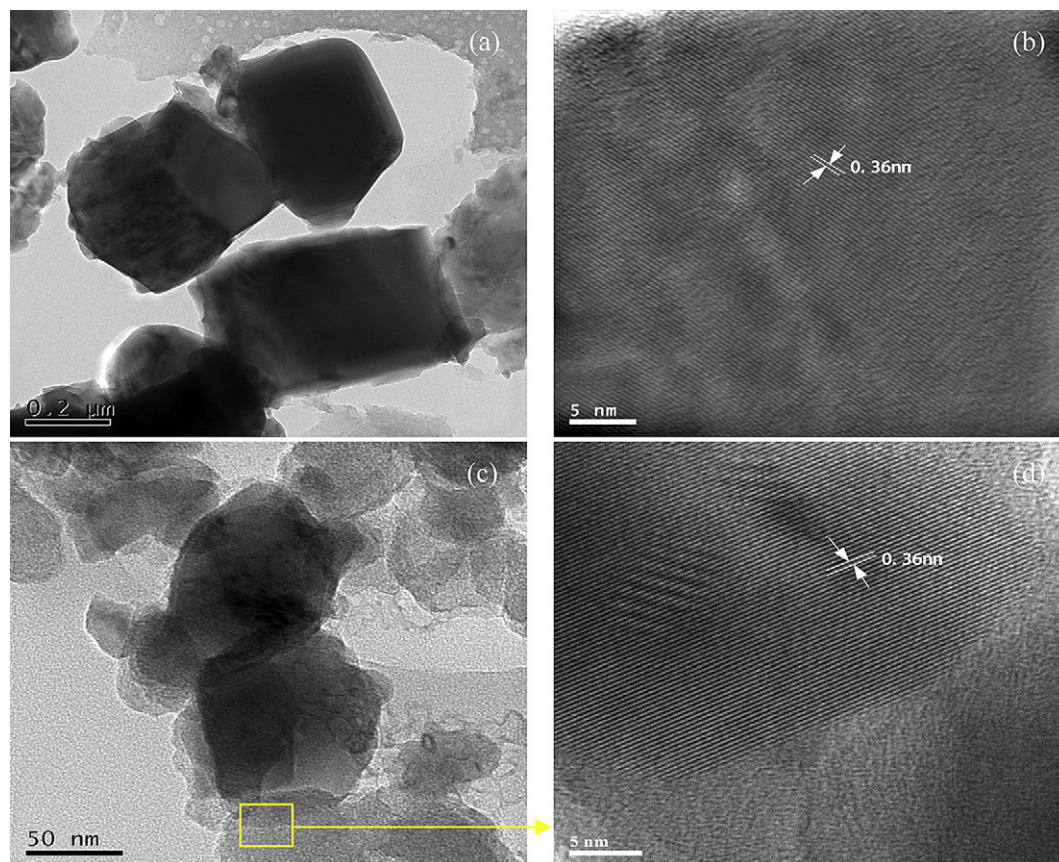


Fig. 4. TEM images of (a) LTP and (c) LTP/C-3; HRTEM images of (b) LTP and (d) LTP/C-3.

H_3PO_4 (formed by the decomposition of $\text{NH}_4\text{H}_2\text{PO}_4$). The pyrolysis reaction of PVA in this region contains a set of complex reactions including Diels–Alder reaction, intramolecular crystallization, and radical reactions, etc. Following that, there is a steep weight loss (around 18%) from 360 to 560 °C, which is attributed to the carbonization of organic residues. With further heating, another slight weight loss about 1 wt% is observed, which is attributed to the formation of $\text{LiTi}_2(\text{PO}_4)_3$.

Fig. 2 shows the XRD patterns of LTP, LTP/C-1, LTP/C-2, LTP/C-3, and LTP/C-4. All the diffraction peaks of the samples could be indexed on the basis of a rhombohedral $\text{LiTi}_2(\text{PO}_4)_3$ structure with a space group of R3c (JCPDS: 35-0754) without any detectable impurity phases. Nevertheless, no detectable reflections corresponding to carbon could be seen in the XRD patterns of LTP/C-1, LTP/C-2, LTP/C-3, and LTP/C-4 due to its low content and amorphous structure. The most common and traditional method to prepare $\text{LiTi}_2(\text{PO}_4)_3$ is the solid-state reaction synthesis. The raw materials should be sintered at 1000 °C until the crystalline $\text{LiTi}_2(\text{PO}_4)_3$ formed. Using this PVA assisted sol–gel method, single phase $\text{LiTi}_2(\text{PO}_4)_3$ can be obtained at a much lower temperature (800 °C) than classic solid-state reaction synthesis. The polyvinyl alcohol (PVA), which is a hydrophilic polymer contributing hydroxyl group on each of its repeating units, generally used as suspension stabilizer, exhibits the effect of reducing particle size of the polymer by decreasing the surface tension and improving the dispersion of the reactants during the polymerization reaction [21]. In this work, PVA is used to form polymer matrix with a whole range of homogeneously trapped reactants in gel and prolongs sedimentation reaction therefore particles trammel in gel pores while the solvent gently evaporates.

The SEM images of LTP, LTP/C-1, LTP/C-2, LTP/C-3, and LTP/C-4 are shown in Fig. 3. The LTP is composed of irregular micrometer-sized particles. The range of particles size is 1–5 μm (see Fig. 3a). The morphology of LTP is completely destroyed by ball-milling with acetylene black. LTP/C-1 includes many sub-microparticles due to the impact of ball-milling, but some large particles haven't been crushed and still exist (see Fig. 3b). This is attributed to the insufficiency of acetylene black. LTP/C-2, LTP/C-3, and LTP/C-4 have more even particles. These composites are composed of sub-microparticles, and few sub-microparticles agglomerate to second particles (see Fig. 3c–e).

To further examine the effect of the ball-milling process, the LTP and LTP/C-3 were observed using a transmission electron microscope. The LTP particles appear to be micrometer-sized and isolate from each other as shown in Fig. 4a. The HRTEM image of LTP is presented in Fig. 4b. It can be indicated that the lattice-fringe distance is about 0.36 nm, corresponding to the (113) d-space of rhombohedral $\text{LiTi}_2(\text{PO}_4)_3$ (JCPDS: 35-0754), which is consistent with the XRD results. It can be seen that particle sizes have been effectively decreased after ball-milling with acetylene black. The particle size of LTP/C-3 is 50–100 nm (see Fig. 4c). TEM image of LTP/C-3 clearly indicates that the particles are of nanostructured sizes, which are closely interwoven with each other across the full field of view. The HRTEM image of LTP/C-3 provides further insight into $\text{LiTi}_2(\text{PO}_4)_3$ particles and acetylene black (see Fig. 4d). The $\text{LiTi}_2(\text{PO}_4)_3$ particles are distinguishable from the acetylene black. Smaller particles will induce shorter diffusion distance of Li^+ ions. Moreover, the acetylene black particles contribute to the form of network, which can interconnect the isolated particles, so that the electrons can be readily transmitted to the sites where redox

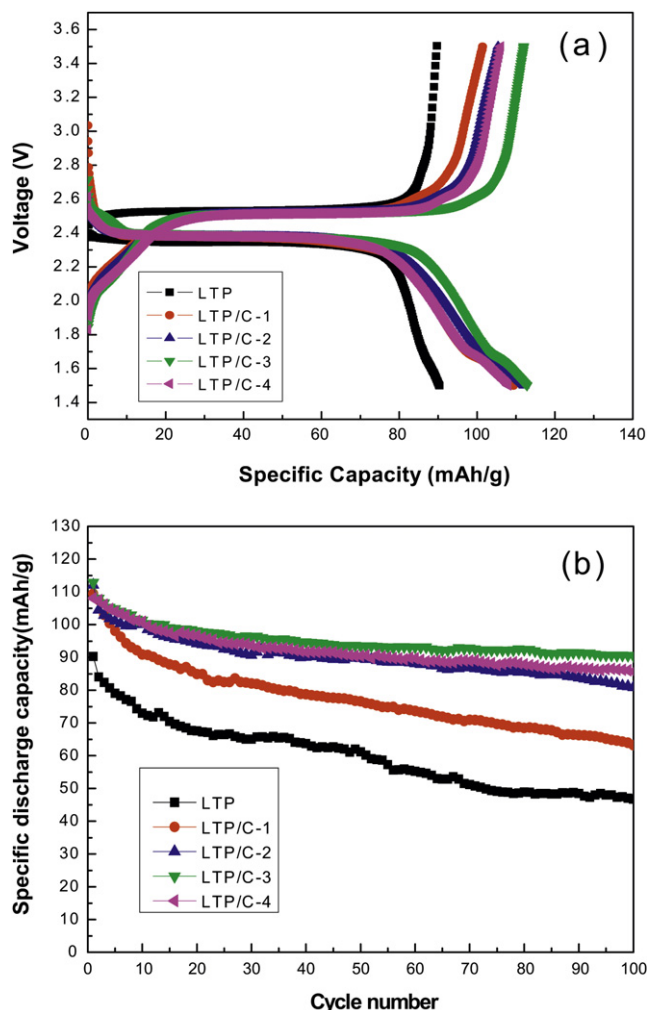


Fig. 5. (a) Initial discharge/charge curves and (b) discharge capacity as a function of cycle number of LTP, LTP/C-1, LTP/C-2, LTP/C-3, and LTP/C-4 at 0.5C.

reactions take place. For these reason, LTP/C-3 has large charge–discharge capacity and rate capability as it will be shown and discussed in the following section.

Initial discharge/charge curves of LTP, LTP/C-1, LTP/C-2, LTP/C-3, and LTP/C-4 at 0.5C are illustrated in Fig. 5a. The shapes of these curves are similar. All samples show the discharge plateau at about 2.4 V and corresponding charge plateau at about 2.5 V, indicating the two-phase reaction of the $\text{LiTi}_2(\text{PO}_4)_3$ and $\text{Li}_3\text{Ti}_2(\text{PO}_4)_3$ system. The initial discharge capacity of LTP is 90.3 mAh g^{-1} . The discharge capacity increases obviously after ball-milling with acetylene black. Initial discharge capacities of LTP/C-1, LTP/C-2, LTP/C-3, and LTP/C-4 are 109.4, 112.2, 112.8, and 108.0 mAh g^{-1} , respectively. The discharge capacity as a function of cycle number of LTP, LTP/C-1, LTP/C-2, LTP/C-3, and LTP/C-4 at 0.5C is shown in Fig. 5b. The discharge capacity of LTP decreased acutely with subsequent cycles, the discharge capacity only remains at 46.7 mAh g^{-1} after 100 cycles. The cycling performance improved remarkably after ball-milling with acetylene black. The discharge capacities of LTP/C-1, LTP/C-2, LTP/C-3, and LTP/C-4 remain at 63.2, 80.9, 90.5, and 85.7 mAh g^{-1} after 100 cycles, respectively. Though the cycling performance of LTP/C-1 is much better than LTP, the capacity fading of LTP/C-1 is quicker than other ball-milled composites. This is due to the amount of acetylene black in the LTP/C-1 is insufficient. LTP/C-3 shows the highest specific capacity and the best cycle performance, so the optimal amount of acetylene black is 15 wt. %.

Fig. 6 compares the rate capabilities (at 0.1–5C rates) of LTP and LTP/C-3. Fig. 6a and b illustrates the initial discharge/charge curves of the LTP and LTP/C-3, respectively, as a function of rate ranging from 0.1 to 5C. The charge–discharge profiles of both samples appear with the typical voltage plateau attributed to the two-phase reaction of the $\text{LiTi}_2(\text{PO}_4)_3$ and $\text{Li}_3\text{Ti}_2(\text{PO}_4)_3$ system. At a slow rate (0.1C), the discharge curves are characterized by a plateau at 2.4 V, which corresponds to the reaction $\text{LiTi}_2(\text{PO}_4)_3 + 2\text{Li}^+ + 2\text{e}^- \rightarrow \text{Li}_3\text{Ti}_2(\text{PO}_4)_3$. At 0.1C, the discharge capacities of LTP and LTP/C-3 are 106.6 and 129.4 mAh g^{-1} , respectively. LTP/C-3 shows higher capacity than LTP. It is clear that, as the current density increases, the specific capacity decreases, while the charge/discharge polarization becomes more pronounced. However, the LTP delivers much lower capacities at high current densities than LTP/C-3; e.g., 64.5 and 87.5 mAh g^{-1} at 5C (700 mA g^{-1}) are obtained for LTP and LTP/C-3, corresponding to 60.5% and 67.6% of their capacities at 0.1C (14 mA g^{-1}) as summarized in Fig. 6c, respectively. The high rate (or fast) charge and discharge capability of LTP/C-3 can be greatly improved because of the reformative kinetics provided by electronically conducting carbon network existed in LTP/C-3.

To further show the advantage of LTP/C-3, a comparison of cycle performance at different C rates between samples LTP and LTP/C-3 was performed and shown in Fig. 7. The LTP/C-3 shows much better cyclic performance than LTP (see Fig. 7a and b). The discharge capacities of LTP after 100 cycles at 0.1, 1.0, 2.0, and 5.0C are only 68.8, 48.6, 38.7, and 24.2 mAh g^{-1} , respectively. However, the discharge capacities of LTP/C-3 after 100 cycles at 0.1, 1.0, 2.0, and 5.0C remain as 106.4, 86.5, 79.9, and 65.6 mAh g^{-1} , respectively. The capacity retentions of LTP/C-3 after 100 cycles are much larger than those of LTP at different C rates (See Fig. 7c). There is an obvious capacity fading after the first cycle for both samples. The capacity retentions of LTP/C-3 after 100 cycles are 83%, 86.2%, 88.2%, 84.8% at 0.1, 1.0, 2.0, and 5.0C (calculated based on the second specific discharge capacity), respectively. The capacity retentions of LTP after 100 cycles are only 74.7%, 68.6%, 61.6%, 44.3% at 0.1, 1.0, 2.0, and 5.0C (calculated based on the second specific discharge capacity), respectively. The data demonstrate the excellent capacity retention of the LTP/C-3 at different C rates. Moreover, the capacity fading becomes acutely with the increase of current density for LTP, indicating poor rate capability. This trend becomes indistinctively for LTP/C-3. LTP/C-3 has much better rate capability than LTP can be deduced. The improved rate performance and cycle stability mainly attributes to three possibilities: (i) Size reduction of particle and a narrow size distribution results in enhancement on ion transport by ball-milling, the chemical diffusion coefficient of lithium in cathode is improved [22,23]. (ii) The AB particles contribute to the form of network, which can interconnect the isolated particles, so that the electrons can be readily transmitted to the sites where redox reactions take place to keep the charge balance. Thereby, the electronic conductivity increase and cell polarization reduce [15,20,24,25]. (iii) Carbon coating layer protects the $\text{LiTi}_2(\text{PO}_4)_3$ active material from contacting with electrolyte directly, thus restrains the partial dissolution of the cathodes as a result of traces of HF in the LiPF_6 electrolyte [24]. It is interesting that capacity fading is somewhat more pronounced for LTP/C-3 at the lower rates. The increased capacity fading at low rates is a common observation in cathode materials with nanostructure and probably results from a combination of increased reactivity toward the electrolyte and prolonged contact between the active material and electrolyte [26]. In any case, the LTP/C-3 exhibits a good electrochemical response in terms of both capacity and cycling properties over a wide range of rate capabilities. It has been demonstrated that both the lithium ion conduction and electronic conduction play a critical role in controlling the electrochemical properties of electrode materials. LTP/C-3 has much smaller particles than LTP, and a smaller lithium

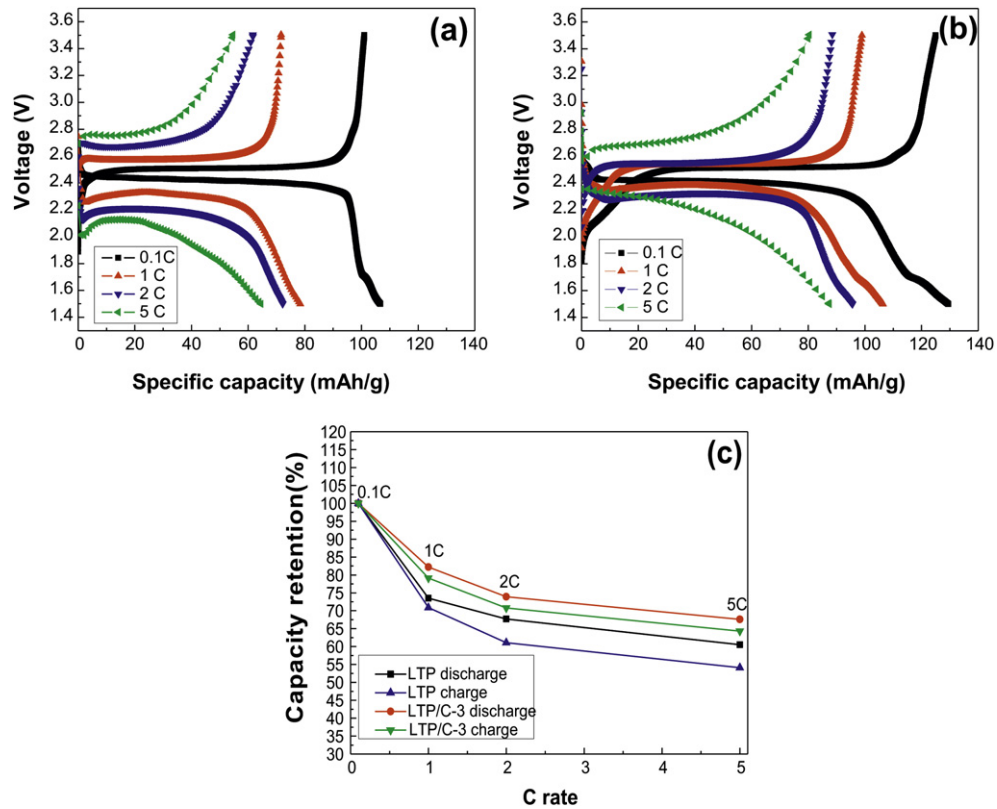


Fig. 6. Initial discharge/charge curves of (a) LTP and (b) LTP/C-3 at various C rates; (c) Capacity remaining ratio of LTP and LTP/C-3 under high C rates as compared to the capacity under 0.1C.

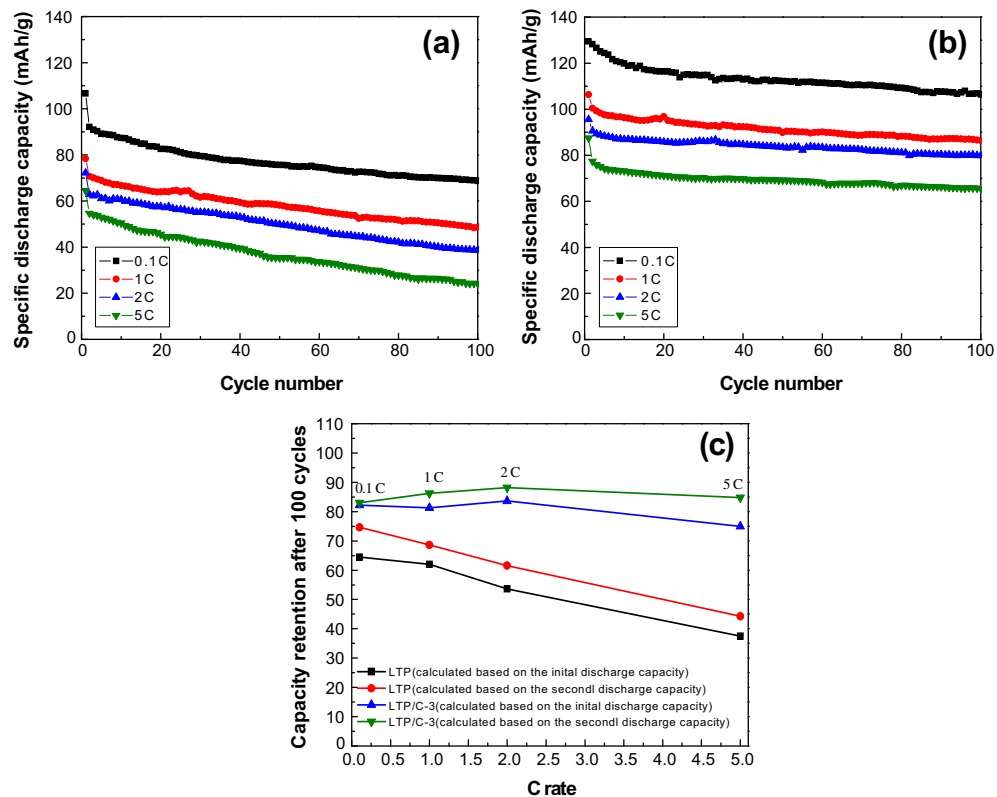


Fig. 7. Discharge capacity as a function of cycle number of (a) LTP and (b) LTP/C-3 at various C rates; (c) Capacity remaining ratio of LTP and LTP/C-3 after 100 cycles under different C rates.

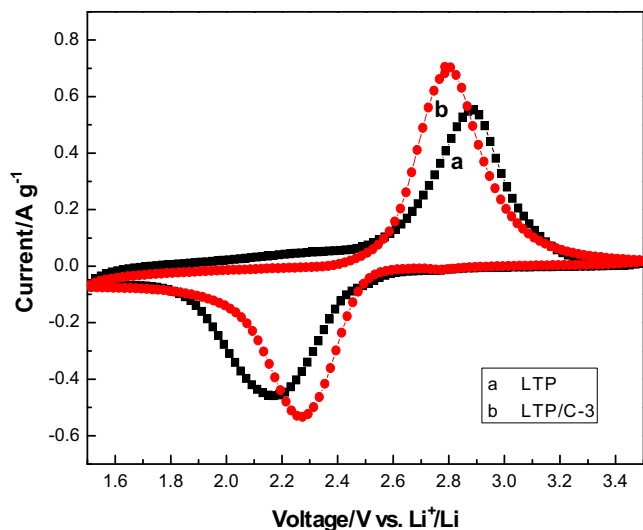


Fig. 8. Cyclic voltammograms of (a) LTP and (b) LTP/C-3 (Scan rate is 1 mV s^{-1}).

diffusion length in the sample will lead to better electrochemical properties. Besides, in LTP/C-3, the uniformly distributed carbon particles formed a network of electrically conductive paths among the $\text{LiTi}_2(\text{PO}_4)_3$ particles, so the active $\text{LiTi}_2(\text{PO}_4)_3$ material can be fully utilized for lithium extraction and insertion reactions.

Fig. 8 compares the cyclic voltammograms of LTP and LTP/C-3. A pair of redox peaks is observed for both samples. The peaks observed in the cathodic sweep and the peak observed in the anodic sweep are characteristic of the insertion and removal of Li into/from the $\text{LiTi}_2(\text{PO}_4)_3/\text{Li}_3\text{Ti}_2(\text{PO}_4)_3$ structure. The redox peaks of LTP are located at 2.171 and 2.889 V, while the redox peaks of LTP/C-3 are located at 2.274 and 2.786 V. The voltage difference between the anodic and the cathodic peaks can reflect the degree of polarization of the electrode. The potential difference between the anodic and cathodic peaks (ΔE_p) of the LTP is found to be 0.718 V, indicating a serious polarization behavior, which is due to the very limited electrical conductivity of the $\text{LiTi}_2(\text{PO}_4)_3$. The LTP/C-3 has the much lower value of ΔE_p (0.512 V) compared with the LTP, showing the weak polarization and good reversibility of the electrode. This is consistent with the excellent rate capability and cycle performance of the LTP/C-3. Moreover, the CV profile of LTP/C-3 exhibits the higher peak current, which facilitates the kinetic process of the electrochemical reactions, indicative of a higher specific capacity. In a word, as compared with the LTP, LTP/C-3 has more

Table 1

EIS parameters for LTP and LTP/C-3.

Samples	R_s (Ω)	R_{ct} (Ω)	CPE-T (F)	CPE-P	$W_0 - R$ (Ω)	$W_0 - t$	$W_0 - P$
LTP	1.815	280	1.2576×10^{-5}	0.81414	401.9	1.052	0.34393
LTP/C-3	1.358	139	2.1324×10^{-5}	0.81794	48.8	0.16853	0.32189

intense anodic and cathodic peaks, less polarization (lower ΔE_p), indicating an improved specific capacity, cycle performance, and rate capability.

The Nyquist plots of the LTP and LTP/C-3 are illustrated in Fig. 9a. An intercept at the Z' axis in high frequency corresponded to the ohmic resistance (R_Ω), which represents the resistance of the electrolyte and electrode material. The semicircle in the middle frequency range indicates the charge transfer resistance (R_{ct}). The inclined line in the low frequency represents the Warburg impedance (W_s), which is associated with the diffusion of lithium ions in the solid matrix. A simplified equivalent circuit model (Fig. 9b) was constructed to analyze the impedance spectra. A constant phase element CPE is placed to represent the double layer capacitance and passive film capacitance. The parameters of the equivalent circuit are recorded in Table 1. It is clear that the R_Ω of LTP/C-3 is 1.358Ω , which is smaller than that of LTP. The R_{ct} of LTP/C-3 is 139Ω , which is much smaller than that of LTP. Therefore, it can be assumed that the electrochemical impedance of LTP/C-3 is smaller than that of LTP. The LTP/C-3 shows much better charge–discharge properties than LTP can be expected.

Galvanostatic intermittent titration technique (GITT) is a powerful tool which can be employed to determine a number of important kinetic and thermodynamic informations in mixed conductors [27]. GITT technique was firstly developed by Weppner and Huggins to determine the diffusion coefficient of Li-ions (D_{Li}) in electrode active materials in Li_3Sb , which combines transient and steady-state measurements [27]. GITT measurements were performed on the second cycle to determine the diffusion coefficient of Li-ions (D_{Li}) in electrode active materials at 25°C . Fig. 10a and b shows the discharge/charge GITT curves of LTP and LTP/C-3 electrodes as a function of time in the potential range of 1.5–3.5 V. The cell was discharged with a constant current flux of 0.1C for an interval of 10 min followed by an open circuit standing for 40 min, allowing the cell voltage to relax to its steady-state value (E_s). The cell voltage can be stabilized to a value after 40 min open-circuit stand after each current flux. Fig. 10c simply illustrates a single step of GITT. Fig. 10d shows an example of an E vs. $t^{1/2}$ plot recorded for LTP/C-3 after application of 0.1C current pulse. It can

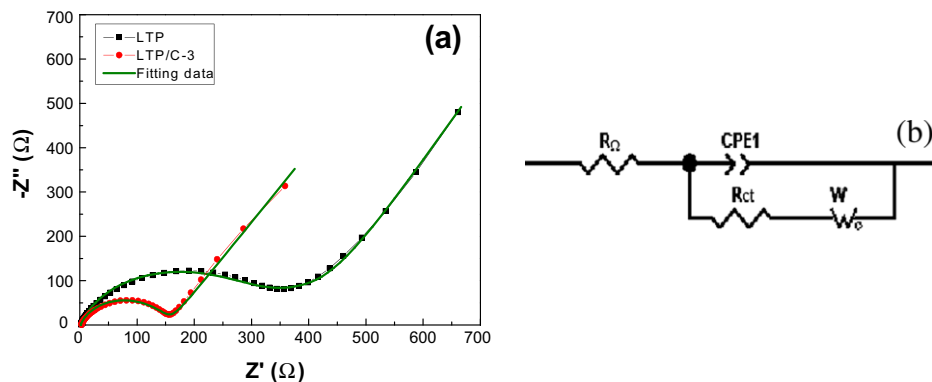


Fig. 9. (a) Nyquist plots of LTP and LTP/C-3; (b) equivalent circuit used for fitting the experimental EIS data; and (c) the relationship plot between Z' and $\omega^{-1/2}$ at low-frequency region.

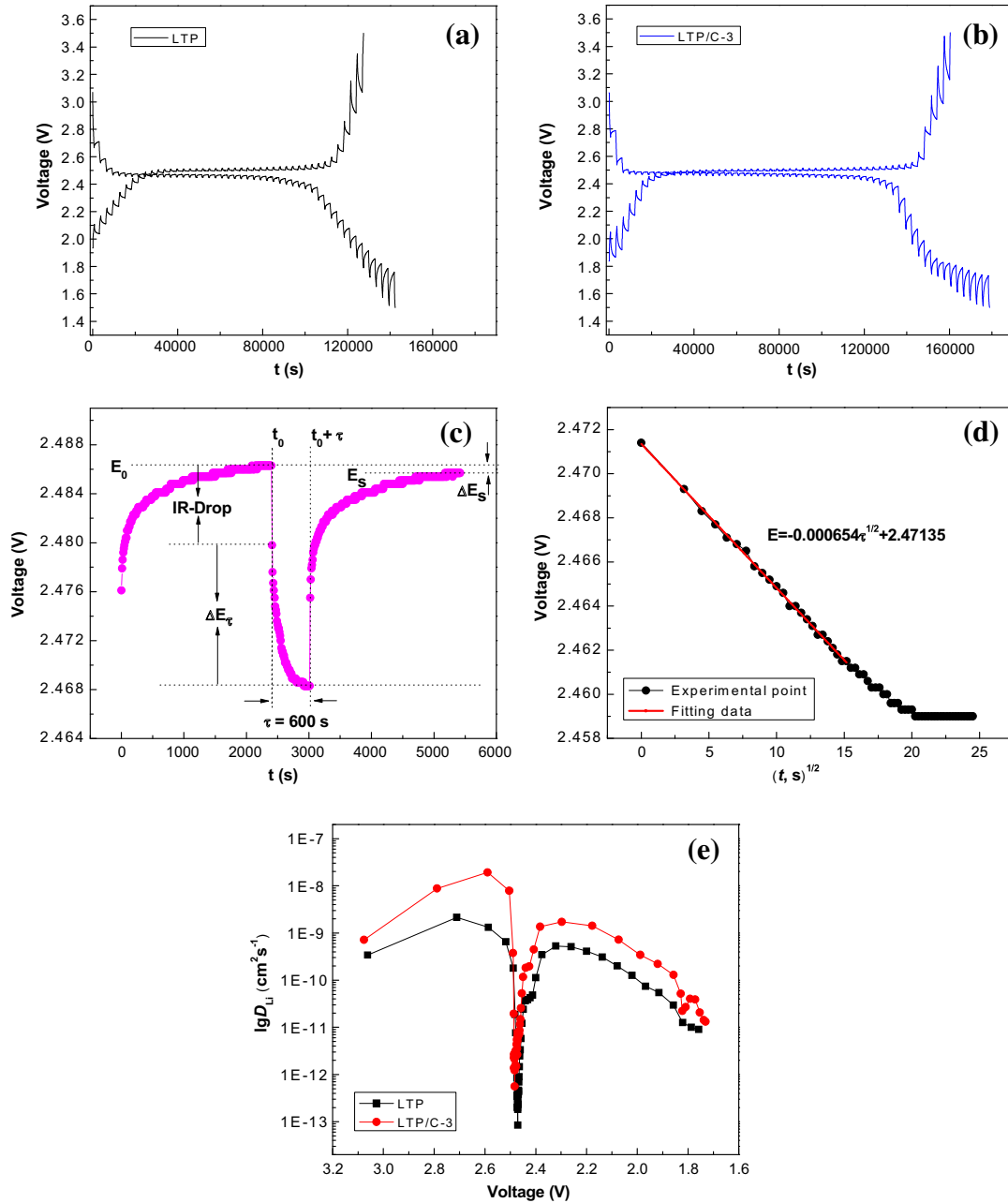


Fig. 10. The discharge/charge GITT curves of LTP (a) and LTP/C-3 electrode (b) as a function of time in the potential range of 1.5–3.5 V. *E* vs. *t* profile of LTP/C-3 electrode for a single GITT during discharge process at 2.48 V with schematic representation of different profile parameters (c). Linear behavior of the transient voltage changes (*E*) vs. (*t*)^{1/2} during a single titration process (d). The calculated *D*_{Li} from the GITT data for LTP and LTP/C-3 as a function of potential during discharge process (e).

be seen that in the time domain from 10 to 100 s, the plot is roughly linear. While the value shows an exponential saturation after 400 s. This is reasonable for the two-phase reaction that the voltage should be constant after short time current polarization. In the literature using GITT techniques [27,28], the time range of 10–100 s is identical. The slope is taken from this linear range to calculate *D*_{Li}. Assuming that lithium transport in the electrode obeys Fick's second law, the chemical diffusion coefficients can be obtained by the following equation [27]:

$$D_{\text{Li}} = \frac{4}{\pi} \left(\frac{I_0 V_m}{S F Z_i} \right)^2 \left(\frac{dE/dx}{dE/dt^{1/2}} \right)^2 \quad (t \ll L^2/D_{\text{Li}}) \quad (1)$$

where *D*_{Li} (cm² s^{−1}) is the chemical diffusion coefficient, *V*_m is the molar volume of LiTi₂(PO₄)₃ (131 cm³ mol^{−1}), *F* is the Faraday

constant (96,485 °C mol^{−1}), *I*₀ (A) is the applied current, *S* (cm²) is the total contact area between the electrolyte and electrodes, *Z*_i is the number of charge transfer, and *L* (cm) is the diffusion length. Based on Eq. (1), the diffusion coefficients Li⁺ ions calculated from the GITT curves as a function of potential are presented in Fig. 10e. The size of the data points is within the error limit of estimation. It is found that the values of *D*_{Li} of LTP are in the range from 8.46 × 10^{−14} to 2.15 × 10^{−9} cm² s^{−1}, while LTP/C-3 are in the range from 5.59 × 10^{−13} to 1.92 × 10^{−8} cm² s^{−1} for Li⁺ ions intercalation. The *D*_{Li} of LTP/C-3 is 7.15 × 10^{−10} cm² s^{−1} at open-circuit voltage (3.08 V vs. Li⁺/Li) and it increases to a maximum of 1.92 × 10^{−8} cm² s^{−1} at 2.59 V, which is higher than that of LTP at the same discharge state. In addition, a minimum can be seen at the middle of the phase transition range for the two samples, implying the same Li⁺ intercalation process. The lithium ion diffusion

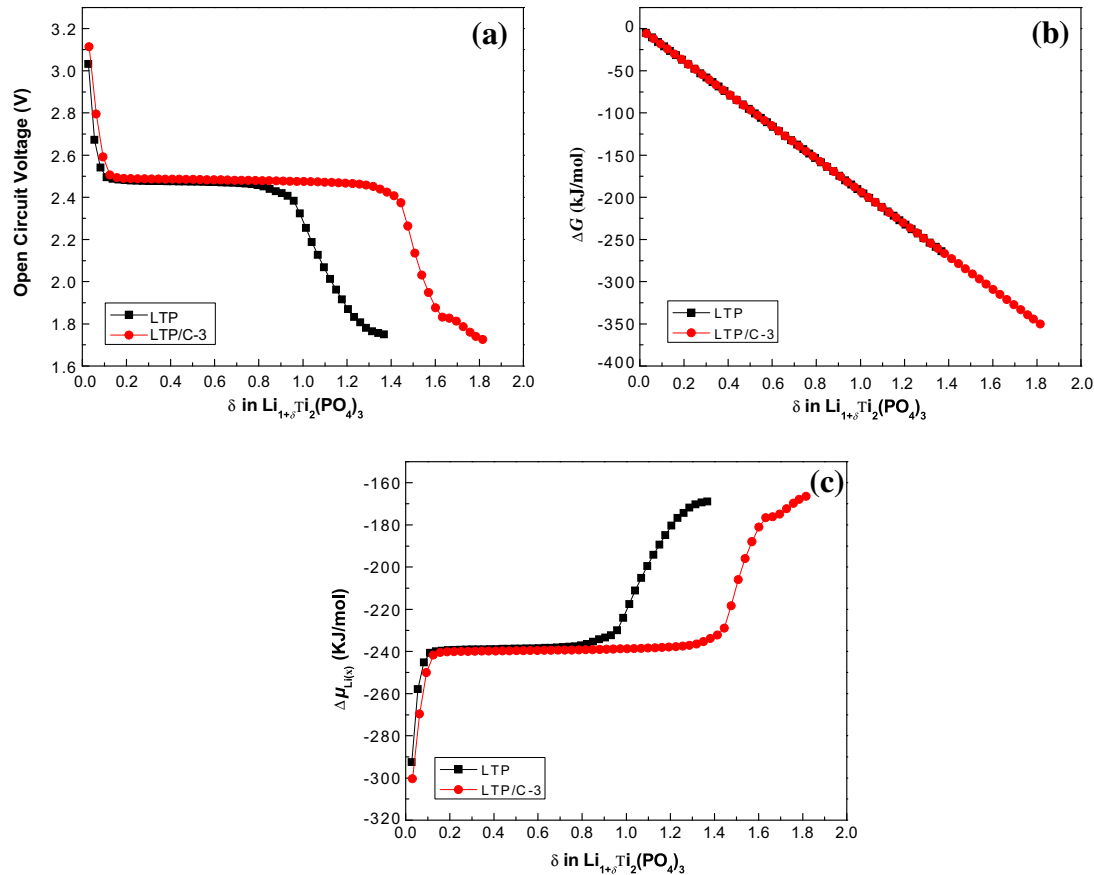
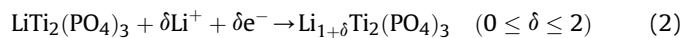


Fig. 11. Coulometric titration curves of $\text{Li}/\text{Li}_{1+\delta}\text{Ti}_2(\text{PO}_4)_3$ cell, the current density was 0.1C and the relaxation condition $\Delta U < 0.5$ mV for a period of time of 300 s (a), standard Gibbs free energy of formation $\text{Li}_{1+\delta}\text{Ti}_2(\text{PO}_4)_3$ (b) and chemical potential of lithium ion in $\text{Li}_{1+\delta}\text{Ti}_2(\text{PO}_4)_3$; and (c) as a function of inserted lithium composition δ in $\text{LiTi}_2(\text{PO}_4)_3$ at 25 °C.

coefficient of LTP/C-3 is much larger than that of LTP. This may be due to effect by the ball-milling with AB, which induces the reduction of particle size and the increase of conductivity by forming uniform electrically conductive carbon network. The interstitials and conducting channels in the NASICON structure could accelerate Li^+ diffusion, thus, induce a high lithium diffusion coefficient.

Fig. 11a shows the coulometric titration curves of $\text{Li}/\text{Li}_{1+\delta}\text{Ti}_2(\text{PO}_4)_3$ electrodes. The steady-state open-circuit cell voltages are plotted as a function of the composition, which was electrochemically changed in situ from pure $\text{LiTi}_2(\text{PO}_4)_3$ to lithium-rich composition with a ratio of about 2, corresponding to the composition within the trilithium compound ($\text{Li}_3\text{Ti}_2(\text{PO}_4)_3$). This voltage is then used to calculate the standard free energy change accompanying the cell reaction. Emphasis was given to the measurement of the thermodynamic properties of the phases $\text{Li}_{1+\delta}\text{Ti}_2(\text{PO}_4)_3$ as a function of their composition. The current density was 0.1C and the equilibrium voltage was taken after each relaxation process under the condition $\Delta U < 0.5$ mV for a period of time of 300 s. It is clearly founded that two single phase regions separated by constant-voltage regions of two-phase mixtures can be clearly identified in both samples. In the discharge process, the reaction of $\text{LiTi}_2(\text{PO}_4)_3$ cathode electrode is as follows:



Gibbs free energy of formation for $\text{Li}_{1+\delta}\text{Ti}_2(\text{PO}_4)_3$, ΔG_i ($\text{Li}_{1+\delta}\text{Ti}_2(\text{PO}_4)_3$), can be evaluated as a function of composition by the integration of the titration curve according to the following expression [29]:

$$\Delta G_i = \Delta G_i(\delta) \quad (3)$$

$$\Delta G_i = -nF \int_0^\delta E(\delta) d\delta \quad (4)$$

Simultaneously, the chemical potential of Lithium ion in $\text{Li}_{1+\delta}\text{Ti}_2(\text{PO}_4)_3$ can also be obtained by equation:

$$\Delta\mu_{\text{Li}(\delta)} = \mu_{\text{Li}(\delta)} - \mu_{\text{Li}(\delta)}^0 = RT \ln \alpha_{\text{Li}(\delta)} = -FE(\delta) \quad (5)$$

$$\alpha_{\text{Li}(\delta)} = \exp\left(-\frac{FE}{RT}\right) \quad (6)$$

While μ_{Li}^0 is the chemical potential of pure Lithium, $\mu_{\text{Li}(\delta)}$ is the chemical potential of Lithium ion in $\text{Li}_{1+\delta}\text{Ti}_2(\text{PO}_4)_3$, $E(\delta)$ is the steady-state open-circuit cell voltage (OCV) at different amount of

Table 2
Thermodynamic data of lithium ion insertion in $\text{Li}_{1+\delta}\text{Ti}_2(\text{PO}_4)_3$ of LTP at 25 °C.

δ	0.1	0.3	0.5	0.7	0.9	1.1	1.3	1.4
OCV (V)	2.54	2.48	2.48	2.47	2.46	2.38	1.96	1.75
ΔG (kJ/mol)	-15.9	-52.9	-84.7	-116.5	-153.5	-185.0	-221.9	-263.9
$\Delta\mu$ (kJ/mol)	-245.2	-239.0	-238.8	-238.5	-237.1	-229.9	-189.4	-170.9

Table 3Thermodynamic data of lithium ion insertion in $\text{Li}_{1+\delta}\text{Ti}_2(\text{PO}_4)_3$ of LTP/C-3 at 25 °C.

δ	0.1	0.3	0.5	0.7	0.9	1.1	1.3	1.5	1.7	1.8
OCV (V)	2.59	2.49	2.48	2.48	2.48	2.47	2.45	2.14	1.81	1.73
ΔG (kJ/mol)	−18.2	−60.6	−97.0	−133.4	−175.8	−212.1	−254.5	−290.9	−327.3	−350.3
$\Delta\mu$ (kJ/mol)	−250.0	−239.9	−239.7	−239.4	−239.0	−238.5	−236.5	−206.0	−174.9	−166.5

Lithium ion insertion, and $\alpha_{\text{Li}(\delta)}$ is the activity of Lithium ion in $\text{Li}_{1+\delta}\text{Ti}_2(\text{PO}_4)_3$. Fig. 11b shows the standard Gibbs free energy of formation $\text{Li}_{1+\delta}\text{Ti}_2(\text{PO}_4)_3$ as a function of the composition at 25 °C evaluated by integration of the coulometric titration curve according to Eq. (4). The standard Gibbs free energy ΔG_i varies almost linearly with the stoichiometric parameter δ . The detailed thermodynamic data are listed in Tables 2 and 3. In the two-phase regions at 2.48 V, ΔG_i is, of course, a linear function of the mole fraction of lithium, as expected. It is seen that the values are negative over the entire range of composition, with a minimum (−350.3 kJ mol^{−1}) at approximately the nominal composition of the phase $\text{Li}_3\text{Ti}_2(\text{PO}_4)_3$ for LTP/C-3, with the maximum amount of lithium ion insertion δ is 1.82. However, for LTP, the minimum value is −263.9 kJ mol^{−1} when the maximum δ is 1.37. Moreover, the chemical potential of Lithium ion $\Delta\mu_{\text{Li}(\delta)}$ in $\text{Li}_{1+\delta}\text{Ti}_2(\text{PO}_4)_3$ of LTP/C-3 (−166.5 kJ mol^{−1}) is higher than that of pure LTP (−170.9 kJ mol^{−1}) when reaching the full discharge, indicating that the activity of Li^+ in LTP/C-3 nanocomposite overtop pure LTP. Therefore, it is easier for lithium ion intercalating into the electrode in LTP/C-3 compound, thus achieve higher discharge capacity.

4. Conclusion

$\text{LiTi}_2(\text{PO}_4)_3$ -AB nanocomposites were synthesized by a PVA assisted sol–gel route followed by ball-milling with acetylene black. It is found that both of the capacity and cycling stability have been promoted notably by ball-milling with acetylene black. The electrochemical test results show that the $\text{LiTi}_2(\text{PO}_4)_3$ -AB nanocomposite with 15 wt% acetylene black exhibits excellent electrochemical performance with the maximum discharge capacity of 129.4, 106.4, 95.6 and 87.5 mAh·g^{−1} at rates of 0.1C, 1C, 2C and 5C in the voltage range of 1.5–3.5 V vs. Li/Li^+ . Meanwhile, it has excellent cycle performance. The carbon coating to suppress the capacity fade observed in the uncoated cells by increasing the electronic conductivity and reducing cell polarization, thus preventing the evolution of oxygen from the cathodes. CV measurements indicate that the improvement of dynamic behavior for $\text{LiTi}_2(\text{PO}_4)_3$ -AB nanocomposite. EIS results show that the electrochemical resistance of $\text{LiTi}_2(\text{PO}_4)_3$ -AB nanocomposite is much smaller than the bare material. GITT tests reveal the Li^+ ions diffusion coefficient of $\text{LiTi}_2(\text{PO}_4)_3$ -AB nanocomposite electrode during lithiation process is enhanced, with a maximum of $1.92 \times 10^{-8} \text{ cm}^2 \text{ s}^{-1}$. Simultaneously, the standard Gibbs free energy ΔG_i of $\text{LiTi}_2(\text{PO}_4)_3$ -AB is −350.3 kJ mol^{−1}, which is smaller than that of pure $\text{LiTi}_2(\text{PO}_4)_3$ (−263.9 kJ mol^{−1}). All experimental phenomenons indicate that the improved properties are attributed to the carbon coating. Smaller particles size, shorter diffusion distance, better

conductivity, and faster kinetics give rise to the outstanding electrochemical performance of $\text{LiTi}_2(\text{PO}_4)_3$ -AB nanocomposites.

Acknowledgments

This study was financially supported by the National Natural Science Foundation of China (grant no. 51202209), the Doctoral Fund of Ministry of Education of China (grant no. 20114301120007), China Postdoctoral Science Foundation (grant no. 20100480954), the Hunan Provincial Natural Science Foundation of China (grant no. 11JJ4038), and Scientific Research Fund of Xiangtan University (grant no. 09XZX10).

References

- [1] M. Catti, A. Comotti, S.D. Blas, R.M. Ibberson, J. Mater. Chem. 14 (2004) 835.
- [2] P. Birke, F. Salam, S. Doring, W. Weppner, Solid State Ionics 118 (1999) 149.
- [3] S. Patoux, C. Masquelier, Chem. Mater. 14 (2002) 5057.
- [4] C. Delmas, A. Nadiri, J.L. Soubeyroux, Solid State Ionics 28–30 (1988) 419.
- [5] C. Delmas, F. Cherkaoui, A. Nadiri, P. Hagemmuller, Mater. Res. Bull. 22 (1987) 631.
- [6] A. Aatiq, C. Delmas, A. El Jazouli, J. Solid State Chem. 158 (2001) 169.
- [7] A. Aatiq, M. Menetrier, L. Croguennec, E. Suard, C. Delmas, J. Mater. Chem. 12 (2002) 2971.
- [8] J.Y. Luo, Y.Y. Xia, Adv. Funct. Mater. 17 (2007) 3877.
- [9] J.Y. Luo, L.J. Chen, Y.J. Zhao, P. He, Y.Y. Xia, J. Power Sources 194 (2009) 1075.
- [10] H. Wang, K. Huang, Y. Zeng, S. Yang, L. Chen, Electrochim. Acta 52 (2007) 3280.
- [11] J. Qian, M. Zhou, Y. Cao, X. Ai, H. Yang, J. Phys. Chem. C 114 (2010) 3477.
- [12] K. Hoang, M. Johannes, Chem. Mater. 23 (2011) 3003.
- [13] C. Sun, S. Rajasekhara, J.B. Goodenough, F. Zhou, J. Am. Chem. Soc. 133 (2011) 2132.
- [14] G.X. Wang, D.H. Bradhurst, S.X. Dou, H.K. Liu, J. Power Sources 124 (2003) 231.
- [15] H. Kim, H. Kim, S.W. Kim, K.Y. Park, J. Kim, S. Jeon, K. Kang, Carbon 50 (2012) 1966.
- [16] F. Badway, N. Pereira, F. Cosandey, G.G. Amatucci, J. Electrochem. Soc. 150 (2003) A1209.
- [17] A. Vu, A. Stein, Chem. Mater. 23 (2011) 3237.
- [18] C. Wessells, R.A. Huggins, Y. Cui, J. Power Sources 196 (2011) 2884.
- [19] V. Aravindan, W. Chuiling, M.V. Reddy, G.V. Subba Rao, B.V.R. Chowdari, S. Madhavi, Phys. Chem. Chem. Phys. 14 (2012) 5808.
- [20] R. Dominko, M. Bele, M. Gaberscek, M. Remskar, D. Hanzel, S. Pejovnik, J. Jamnik, J. Electrochem. Soc. 152 (2005) A607.
- [21] H. Karami, F. Taala, J. Power Sources 196 (2011) 6400.
- [22] P.P. Prosini, M. Lisi, D. Zane, M. Pasquali, Solid State Ionics 148 (2002) 45.
- [23] V. Srinivasan, J. Newman, J. Electrochem. Soc. 151 (2004) A1517.
- [24] B.L. Cushing, J.B. Goodenough, Solid State Sci. 4 (2002) 1487.
- [25] T. Drezen, N.H. Kwon, P. Bowen, I. Teerlinck, M. Isono, I. Exnar, J. Power Sources 174 (2007) 949.
- [26] J.C. Arrebola, A. Caballero, M. Cruz, L. Hernán, J. Morales, E.R. Castellón, Adv. Funct. Mater. 16 (2006) 1904.
- [27] W. Weppner, R.A. Huggins, J. Electrochem. Soc. 124 (1977) 1569.
- [28] R. Amin, J. Maier, P. Balaya, D.P. Chen, C.T. Lin, Solid State Ionics 179 (2008) 1683.
- [29] W. Weppner, R.A. Huggins, J. Electrochem. Soc. 125 (7) (1978).